

## Intermolecular coupling enhanced thermopower in single-molecule diketopyrrolopyrrole junctions

Journal:	<i>National Science Open</i>
Manuscript ID	NSO20220033.R2
Manuscript Type:	Research Article
Date Submitted by the Author:	11-Oct-2022
Complete List of Authors:	Fang, Chao; Xiamen University Almughathawi, Renad; Lancaster University Wu, Qingqing; Lancaster University Cao, Wenqiang; Xiamen University Chen, Hang; Xiamen University Hou, Songjun ; Lancaster University Gu, Yu; Lancaster University Zhang, Hwei; Xiamen University Zhao, Yi; Xiamen University Zheng, Jueting; Xiamen University Li, Guopeng; Xiamen University Shi, Jia; Xiamen University Liu, Junyang; Xiamen University Mao, Bing-Wei; Xiamen University Liu, Zitong; Lanzhou University Lambert, Colin; Lancaster University Hong, Wenjing; Xiamen University
Keywords:	single-molecule electronics, single-molecule junctions, thermopower, thermoelectric devices, intermolecular coupling

SCHOLARONE™  
Manuscripts

Chemistry

## Intermolecular coupling enhanced thermopower in single-molecule diketopyrrolopyrrole junctions

Chao Fang<sup>1,#</sup>, Renad Almughathawi<sup>2,6,#</sup>, Qingqing Wu<sup>2,#</sup>, Wenqiang Cao<sup>1,#</sup>, Hang Chen<sup>1,#</sup>, Songjun Hou<sup>2</sup>, Yu Gu<sup>1</sup>, Hwei Zhang<sup>1</sup>, Yi Zhao<sup>1</sup>, Jueting Zheng<sup>1</sup>, Guopeng Li<sup>1</sup>, Jia Shi<sup>1</sup>, Junyang Liu<sup>1,4</sup>, Bing-Wei Mao<sup>1</sup>, Zitong Liu<sup>3,5,\*</sup>, Colin J. Lambert<sup>2,\*</sup>, Wenjing Hong<sup>1,4,5,\*</sup>

<sup>1</sup>State Key Laboratory of Physical Chemistry of Solid Surfaces, College of Chemistry and Chemical Engineering, Xiamen University, Xiamen 361005, China;

<sup>2</sup>Department of Physics, Lancaster University, LA1 4YB, Lancaster, UK;

<sup>3</sup>State Key Laboratory of Applied Organic Chemistry (SKLAOC), College of Chemistry and Chemical Engineering, Lanzhou University, Lanzhou, 730000, P. R. China;

<sup>4</sup>Innovation Laboratory for Sciences and Technologies of Energy Materials of Fujian Province (IKKEM), Xiamen 361005, China;

<sup>5</sup>Beijing National Laboratory for Molecular Sciences, 100190 Beijing, P. R. China

<sup>6</sup>Department of physics, Faculty of Science, Taibah University, Madinah, Saudi Arabia.

#Contributed equally to this work.

\*Corresponding authors (emails: [liuzt@lzu.edu.cn](mailto:liuzt@lzu.edu.cn) (Zitong Liu); [c.lambert@lancaster.ac.uk](mailto:c.lambert@lancaster.ac.uk) (Colin J. Lambert); [whong@xmu.edu.cn](mailto:whong@xmu.edu.cn) (Wenjing Hong))

Received 15 May 2022; Revised 11 October 2022; Accepted 11 October 2022

**Abstract:** Sorting out organic molecules with high thermopower is essential for understanding molecular thermoelectrics. The intermolecular coupling offers a unique chance to enhance the thermopower by tuning the bandgap structure of molecular devices, but the investigation of the intermolecular coupling in bulk materials remains challenging. Herein, we investigated the thermopower of diketopyrrolopyrrole (DPP) cored single-molecule junctions with different coupling strengths by varying the packing density of the self-assembled monolayers (SAM) using a customized scanning tunneling microscope break junction (STM-BJ) technique. We found that the thermopower of DPP molecules could be enhanced up to one order of magnitude with increasing packing density, suggesting that the thermopower increases with larger neighboring intermolecular interactions. The combined density functional theory (DFT) calculations revealed that the closely-packed configuration brings stronger intermolecular coupling and then reduces the HOMO-LUMO gap, leading to an enhanced thermopower. Our findings offer a new strategy for developing organic thermoelectric devices with high thermopower.

**Keywords:** single-molecule electronics, single-molecule junctions, thermopower, thermoelectric devices, intermolecular coupling

### INTRODUCTION

Thermoelectric materials offer the opportunity for direct conversion of heat into electric energy via Seebeck effects [1-4], and the efficiency of thermoelectric devices can be evaluated through the dimensionless figure of merit  $ZT = GS^2T/\kappa$ , where  $G$  is the electrical conductance,  $S$  is the Seebeck coefficient,  $T$  is the temperature, and  $\kappa = \kappa_{el} + \kappa_{ph}$  is the thermal conductance due to electrons ( $\kappa_{el}$ ) and phonons ( $\kappa_{ph}$ ) [5]. Compared with inorganic thermoelectric materials, molecular thermoelectric materials exhibit lower thermal conductivity ( $\kappa_{ph}$ ) and higher flexibility with tunable electronic structures [6-9], some pioneering theoretical works even suggested that molecular thermoelectric devices can reach the highest  $ZT$  value up to be 5.9 [10]. However, the experimental determined Seebeck coefficients of the molecule-scale thermoelectric materials are still much lower than theoretical predictions [11-13]. Strategies to enhance the Seebeck coefficient are crucial for developing high thermoelectric performance devices at the single-molecule scale.

To increase the  $ZT$  of the molecular devices [14], various strategies have been investigated to improve

the thermopower, including varying molecular length of organic building blocks [11, 15, 16], changing connectivity of molecular cores [17-20], tuning molecule-electrode coupling [21], exploring different anchor groups [22] and substituent groups [23], etc. More importantly, theoretical advances revealed that the intermolecular interactions, such as  $\pi$ - $\pi$  stacking, will enhance  $ZT$  by suppressing the phonon contribution to lowering the thermal conductance [12], suggesting that the intermolecular interactions are essential for the design of molecular devices with high  $ZT$  [24, 25]. However, the role of intermolecular interactions in the thermopower of molecular devices has not yet been experimentally investigated, which is mainly due to the challenges in the control of intermolecular interactions at the single-molecule level. Previous studies have demonstrated that the  $\pi$ - $\pi$  interaction between the porphyrins in the mixed self-assembled monolayers (SAMs) decreases with reducing the concentration of porphyrin during the assembling process [26], which offers the strategy to tune intermolecular couplings by varying packing density in the SAMs and explore how the presence of intermolecular coupling affect the thermoelectric properties from molecular level [27-29].

In this work, we investigated the Seebeck coefficient of diketopyrrolopyrrole (DPP) molecular junctions by varying the packing density of their SAMs. The three target DPPs of difuranyl-DPP (**F-DPP**), dithienyl-DPP (**T-DPP**), dithiazolyl-DPP (**Thia-DPP**) with *p*-methylthiobenzenes at both ends were shown in Figure 1A. To explore the effect of packing density on thermoelectric properties of the single-molecule junctions, we assembled the molecule on a gold surface through immersion in different solutions with different concentrations [30]. We found that the Seebeck coefficients of all DPPs increase with growing molecular packing density. Besides, density functional theory (DFT) based calculations revealed that stronger intermolecular coupling associated with higher packing densities generally reduces the energy gap and leads to an enhanced thermopower on DPP molecules.

## RESULTS

A customized scanning tunneling microscope break junction (STM-BJ) instrument [31, 32] was used to simultaneously measure the conductance and thermopower of the single-molecule junctions at room temperature (Figure 1b). A Peltier device mounted under the substrate was used as a heater to establish a stable temperature difference ( $\Delta T = T_{\text{substrate}} - T_{\text{tip}}$ ) between the tip (at room temperature,  $\sim 298$  K) and the substrate (heated) [11, 33]. The thermopower measurement was performed for four temperature differences ( $\Delta T = 0, 5, 10$  and  $15$  K). To obtain a statistical distribution of  $\Delta V$  of an Au-Molecule-Au junction, we have collected more than 1000 consecutive data at each  $\Delta T$  and selected those that sustained a molecular junction through the entire “hold” period (See SI section 3 for more details).

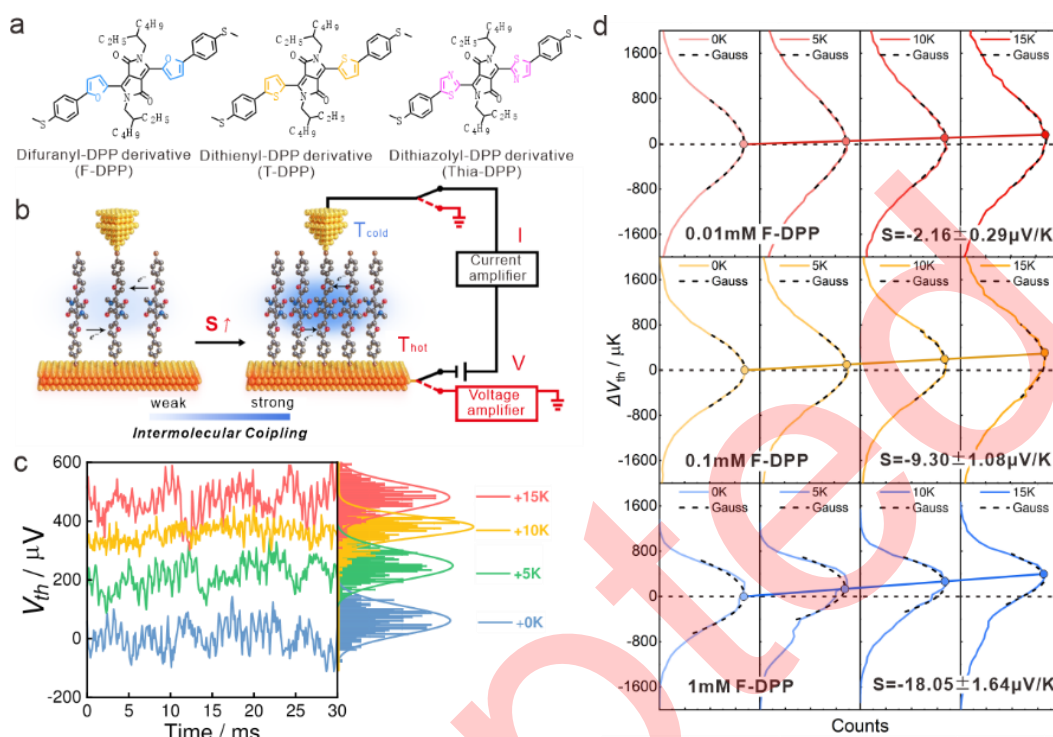


**Figure 1. Schematic diagram of experimental setup and Seebeck coefficient measurement.**

(a) Molecular structures of DPP derivatives studied in this work.

(b) Schematic of the experimental setup. Closely packed molecules enhance the Seebeck coefficient due to stronger intermolecular coupling.

(c) Typical measured individual thermovoltage traces and histograms for single **F-DPP** molecule with 1mM immersion concentration at a series of  $\Delta T$  (0 K, 5 K, 10 K, and 15 K).

(d) Histograms of single **F-DPP** molecule thermoelectric voltage measurements with different immersion concentrations (0.01 mM, 0.1 mM, 1 mM). Gaussian fits were plotted in a black dash curve. The horizontal black dash line indicates the baseline of thermoelectric voltage at  $\Delta V_{th} = 0$ . The Seebeck coefficients were obtained from the thermovoltage as a function of  $\Delta T$ . Solid lines are the linear fitting.

The typical individual thermovoltage traces and histograms are shown in Figure 1c for single **F-DPP** molecule (1mM immersion concentration). It is found that a larger temperature difference brings significantly higher  $\Delta V$ , which could be further demonstrated at the distribution histograms of the individual traces (right panel of Figure 1c). To quantitatively determine the Seebeck coefficient, we constructed the distribution histograms of thermovoltage at different temperature differences (Figure 1d) from more than 1000 individual traces, and the most probable thermovoltage could be determined from the Gaussian fitting of the distribution. Because the fluctuation of the molecular junction configurations inevitably occurs during the measurement process, the thermoelectric voltage from different trapped molecular junctions might exhibit different distributions [11]. By fitting the slope of the most-probable thermovoltage value versus the temperature differences, the Seebeck coefficient could be determined to be  $-18.05 \pm 1.64 \mu\text{V/K}$  (See SI section 3 for more measuring and data processing details).

To investigate the role of packing density in SAMs, the Seebeck coefficient was measured for **F-DPP** with increasing packing densities through immersing the gold electrode into corresponding 0.01 mM, 0.1 mM, and 1.0 mM molecule solutions. The previous work had revealed that molecular interaction in the SAMs could be controlled by modulating the concentration of solution during the assembling process [26]. The X-ray photoelectron spectroscopy (XPS) semiquantitative analysis was conducted to confirm chemical composition of molecular monolayer and its atomic ratio [34]. The results suggest that more molecules existed on the gold sample under the immersion of the molecule solutions with increased concentration, based on the atomic concentration of the S 2p peak signal (See SI section 2.2.2 for more details), and the XPS analysis indeed had demonstrated the formation of Au-S bonds in the SAMs.

Besides, analytical electrochemistry was also used to quantitatively determine how much gold surface was covered with **F-DPP** molecules at different immersion concentrations, according to a method modified from a previously published work [35]. The gold electrode with molecules assembled on was used as a working electrode, and a cyclic voltammetry (CV) was performed in 2.5 mM  $K_3Fe(CN)_6/K_4Fe(CN)_6$  solution containing 0.1 M  $KNO_3$  as the supporting electrolyte with a sweep rate of 100 mV/s, and the potential was controlled between -0.2 to 0.6 V to avoid other redox reactions from assembled **F-DPP**. A typical CV at different immersion concentrations was obtained (Figure 2a), there are apparent redox peaks from  $K_3Fe(CN)_6/K_4Fe(CN)_6$  in all cases. The current at the region with potential over redox peak was mainly controlled by reactants diffusion, and the diffusion areas could be obtained by applying the Cottrell equation [36] (See SI section 2.2.1 for more details). The diffusion areas of the bare gold electrode (without molecules assembled) were determined to be  $0.0051\text{ cm}^2$ , while it decreased to  $0.0036\text{ cm}^2$  for molecule-assembled gold electrode with 1mM immersion concentration (Table 1). The diffusion areas could reflect the assembled-molecule-occupied electrode areas, because SAMs with higher packing density left fewer areas for redox reaction and diffusion. Finally, the SAM surface coverage fraction of assembled molecules with different immersion concentrations was obtained according to the diffusion area compared to bare gold (Table 1 and inset of Figure 2b), varying from 7.84% (0.01 mM immersed F-DPP) to 29.41% (1 mM immersed F-DPP). In addition, a micro thermal gravimetric analyzer ( $\mu$ -TGA) [37] was also applied to determine their packing density differences (See SI Section 2.2.3 for more details). All these characterizations indeed proved that the packing density could be controlled by modulating the immersion concentration during the assembling process.

**Table 1.** Immersion concentration-dependent surface coverage of **F-DPP** SAMs

Immersion concentration	CV analysis for SAM surface coverage	
	Diffusion area from Cottrell equation( $\text{cm}^2$ )	SAM fraction of surface coverage (%)
0	0.0051	0
0.01 mM	0.0047	7.84
0.1 mM	0.0045	11.76
1 mM	0.0036	29.41

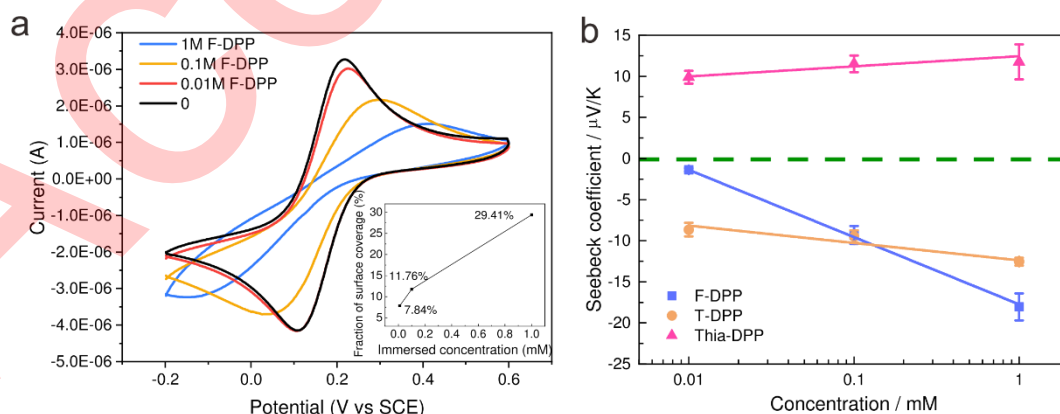


**Figure 2.** CV characterization on SAM surface coverage and Seebeck coefficient of three types of DPP

(a) CV measurements with **F-DPP** assembled gold as the working electrode at different immersion concentrations in 2.5 mM  $K_3Fe(CN)_6/K_4Fe(CN)_6$  containing 0.1 M  $KNO_3$  as the supporting electrolyte, standard calomel and Pt working as reference and counter electrode respectively. (Inset: surface coverage fraction of self-assembled **F-DPP** as a function of immersion concentration.)

(b) Experimentally measured Seebeck coefficient value for **F-DPP** (blue squares), **T-DPP** (brown circles) and **Thia-DPP** (magenta triangles). Error bars are the standard deviation in Gaussian fitting of thermoelectric voltages. The solid line indicates that the absolute Seebeck coefficient of the three DPPs increases with solution concentration. The green dashed line indicated that the Seebeck coefficient  $S = 0$ .

It is found that the Seebeck coefficients of a single **F-DPP** molecule at increasing packing densities are  $-2.16 \pm 0.29\ \mu\text{V/K}$  (0.01 mM),  $-9.30 \pm 1.08\ \mu\text{V/K}$  (0.1 mM) and  $-18.05 \pm 1.64\ \mu\text{V/K}$  (1 mM) (Figure 2b and Table 2). These showed that the Seebeck coefficients of **F-DPP** maintain the same sign (negative) and

increase dramatically with the increase of molecular packing density. More importantly, the Seebeck coefficient of the single-molecule junction could be enhanced near one order of magnitude, which is much larger than the mainstream tuning method called destructive quantum interference (DQI) with only two times enhancement up to now [20]. Furthermore, we observed a similar trend for **T-DPP** and **Thia-DPP**. The Seebeck coefficient of **T-DPP** varied from  $-8.65 \pm 0.82 \mu\text{V/K}$  (0.01mM) to  $-12.55 \pm 0.47 \mu\text{V/K}$  (1mM), and **Thia-DPP** varied from  $+9.89 \pm 0.77 \mu\text{V/K}$  (0.01mM) to  $+11.76 \pm 2.12 \mu\text{V/K}$  (1mM) (See SI section 3 for more details). Interestingly, the sign of the Seebeck coefficient of **Thia-DPP** is opposite to **F-DPP** and **T-DPP**, meaning that altering the adjacent aromatic rings of the DPP core can influence the dominant frontier orbital of charge transport through the molecules. The negative Seebeck coefficient suggested that the Fermi level ( $E_F$ ) of **F-DPP** and **T-DPP** is closer to the LUMO level, and the transport is electron-dominated; the positive Seebeck coefficient suggested that the  $E_F$  of **Thia-DPP** is closer to the HOMO level, and transport is hole-dominated [38]. This trend is as same as that observed in oxidized oligothiophenes derivatives, in which the dominant charge carriers changed from holes to electrons with increasing molecular length [16].

**Table 2.** Single-molecule Seebeck coefficient and conductance measurements.

Compounds with different immersion concentration	Seebeck coefficient ( $\mu\text{V/K}$ )	Measured Conductance ( $\log(G/G_0)$ )
0.01 mM <b>F-DPP</b>	$-2.16 \pm 0.29$	-4.03
0.1 mM <b>F-DPP</b>	$-9.30 \pm 1.08$	-4.00
1 mM <b>F-DPP</b>	$-18.05 \pm 1.64$	-3.93
0.01 mM <b>T-DPP</b>	$-8.65 \pm 0.82$	-4.44
0.1 mM <b>T-DPP</b>	$-9.47 \pm 0.74$	-4.39
1 mM <b>T-DPP</b>	$-12.55 \pm 0.47$	-4.21
0.01 mM <b>Thia-DPP</b>	$+9.89 \pm 0.77$	-4.52
0.1 mM <b>Thia-DPP</b>	$+11.53 \pm 1.01$	-4.47
1 mM <b>Thia-DPP</b>	$+11.76 \pm 2.12$	-4.41

To elucidate the origin of the experimentally observed trends, we investigated the transport properties of **F-DPP**, **T-DPP** and **Thia-DPP** junctions connected to the gold source and drain electrodes via -SMe groups as shown in Figure 3a-c (See more binding configurations for **F-DPP**, **T-DPP** and **Thia-DPP** in SI Figure S9-S11) using DFT combined quantum transport theory (see SI section 4). The material-specific mean-field Hamiltonian of each geometry obtained from SIESTA [39] was combined with quantum transport code Gollum [40] to obtain the electronic transmission coefficient, which controls electrical and thermoelectric properties.

To investigate the dependence of conductance and Seebeck coefficients on the packing density, we calculated the transport properties for junctions containing either a single-molecule (i.e., a monomer junction) or in the presence of two nearby molecules (i.e., optimized geometry of trimer junction is shown in Figure 3a-c). We found that the trimer junctions have smaller HOMO-LUMO gaps than monomers due to the splitting of HOMO and LUMO peaks caused by the interaction with nearby molecules [41]. The modelling demonstrates that the reduced HOMO-LUMO gap of the trimer generally increases the slope of transmission coefficients. Consequently, for a wide range of Fermi energies within the HOMO-LUMO gaps, the Seebeck coefficients of trimers are greater than or equal to monomers, and trimers have similar or higher conductance than the monomers (See SI Figure S9-S12 for more details). These features are in qualitative agreement with the observed experimental trends (See SI Figures S5 and S6 for conductance measurements). DFT has difficulties in predicting the correct HOMO-LUMO gaps [42], charge transfer and Coulomb interaction for charged systems and particularly for these strong acceptor DPP-cores [43, 44]. On the other hand, the Fermi energy is located somewhere inside the HOMO-LUMO gap. Therefore, to compare results for monomer and

trimer molecular junctions, we aligned their mid-gap of the conductance curve (Figure 3d-f). The electrical conductance for **F-DPP** trimer (solid curve) and **F-DPP** monomer (dotted curve) remain in the same value (close to  $10^{-4} G_0$ ), and those for **T-DPP**, **Thia-DPP** trimers and **T-DPP**, **Thia-DPP** monomers possess the conductance around  $10^{-4}$ - $10^{-4.5} G_0$ , which demonstrated a considerable consistency with the experimental data.

The corresponding Seebeck coefficients are displayed in Figure 3g-i. In terms of the net Voronoi charge distribution shown in Table S2, the **Thia-DPP** molecule gains more electrons than **F-DPP** and **T-DPP**, which could induce more vital Coulomb interaction for the negatively charged molecule, moving the energy levels upwards and pushing the HOMO closer to the Fermi energy. Indeed, if the Fermi energy is slightly below the mid-gap position for **Thia-DPP**, then the sign of the Seebeck coefficient would be positive, as shown to the left of the crossing point ( $S = 0$  and  $E_F = -0.3$  eV) in the Seebeck plot of Figure 3i, which also reveals a higher Seebeck coefficient for the trimer junctions. Conversely, for **F-DPP** and **T-DPP**, the right sides of the crossing point of  $S = 0$  have a negative Seebeck coefficient and greater magnitudes for the trimers (Figure 3g and Figure 3h). Figure 3g-i clearly showed that the Seebeck coefficient for the trimer junctions (solid lines) typically has a higher magnitude than the monomers (dotted lines), in agreement with the experimental trends.

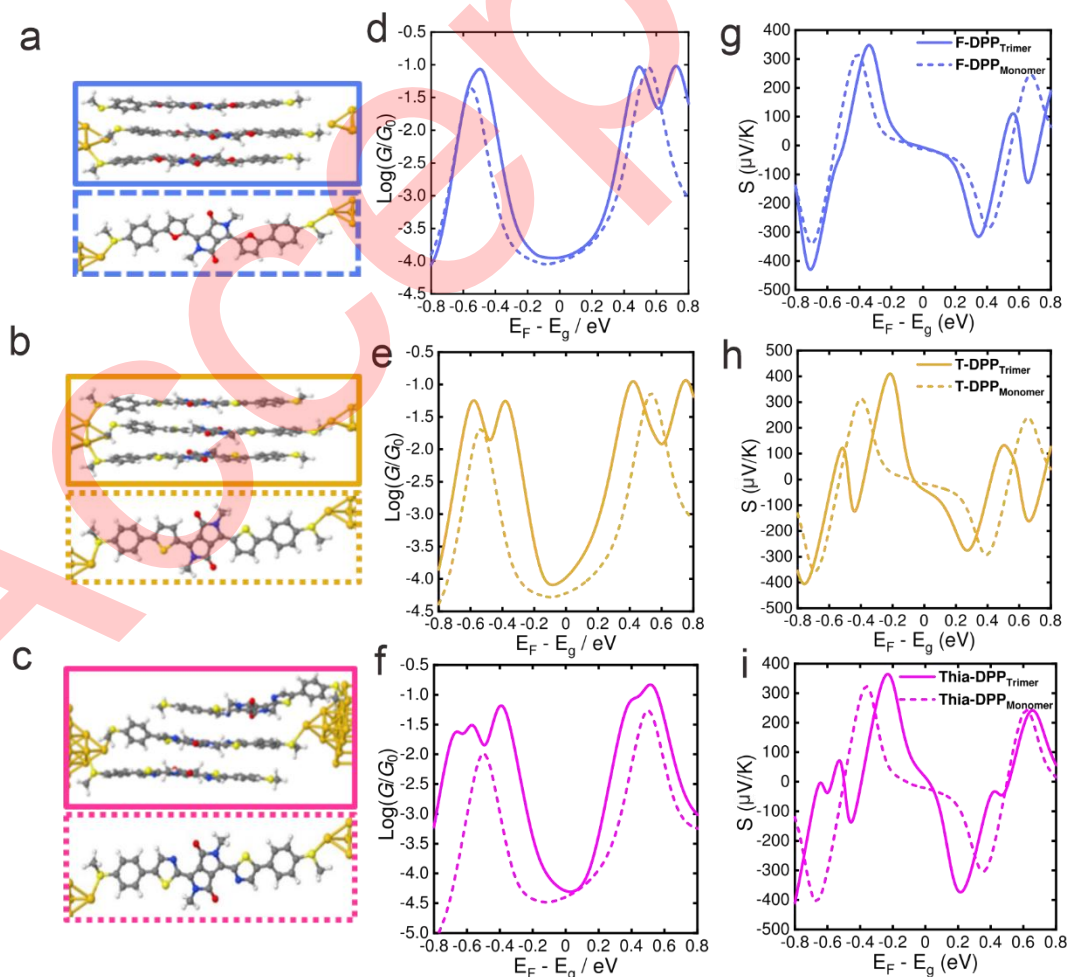


**Figure 3.** DFT calculated electrical and thermoelectric properties of the three DPP derivatives attached to gold electrodes via -SMe anchor groups, the distance between the central backbone and adjacent molecules is around 3.3 to 3.6 Å for **F-DPP**, **T-DPP** and **Thia-DPP** trimers.

(a-i) Models for **F-DPP**, **T-DPP** and **Thia-DPP** respectively. The solid line corresponds to three molecules in the junction (i.e., a trimer), and the dotted line corresponds to a single molecule in the junction (i.e., a monomer).

(d-f) The calculated room-temperature electrical conductance of **F-DPP**, **T-DPP** and **Thia-DPP** as a function of the Fermi energy  $E_F$  relative to the Mid-Gap  $E_g$ . The solid lines represent trimers and dashed lines represent monomers.

(g-i) The calculated room-temperature Seebeck coefficients of **F-DPP**, **T-DPP** and **Thia-DPP** as a function of Fermi energy  $E_F$  with the same shifting corresponding to conductance. The solid lines represent trimers and dashed lines represent monomers.

## DISCUSSION

In conclusion, we experimentally investigated the Seebeck coefficients of a series of single DPP derivatives varying the packing density of SAMs on electrode surface using a modified STM-BJ technique. We discovered that the conductance channel of molecules could be changed from LUMO-dominated to HOMO-dominated by altering the adjacent aromatic rings of the DPP core. More importantly, the thermopower of molecular junctions could be enhanced by up to one order of magnitude via the increase of the packing density in SAMs. Combined DFT calculation revealed that the higher packing density leads to more substantial intermolecular coupling effects, which reduces the HOMO-LUMO gap and increases the Seebeck coefficient. Our results revealed that intermolecular coupling is of fundamental importance for designing highly efficient molecular thermoelectric devices and materials in the future.

## MATERIALS AND METHODS

### Materials

The target molecules were synthesized according to the previous reports [45-47]. For more details, see section S1.1. To obtain SAMs of different packing densities, the gold substrates, which are prepared by coating 200 nm Au film on silicon wafers, were immersed into 0.01, 0.1, 1 mM molecule solution using the solvent of 1,2,4-trichlorobenzene (TCB, 99.9%, Sigma Aldrich) for 4 hours. After that, the surface of the gold substrates with the assembled monolayer was rinsed by TCB and dried with  $N_2$  gas.

### Single-molecule conductance and Seebeck coefficient measurement

The single-molecule conductance and Seebeck coefficient measurements were performed using the home-built STM-BJ technique as described in previous reports [31]. The temperature was modulated by Proportion Integral Differential (PID) control. Single-molecule junctions were fabricated following the electrical conductance measurement [48]. Once the conductance plateau was determined, the tip would be hovered and the tip/substrate distance fixed, followed by cutting off the bias voltage and the current amplifier. Instead, the voltage amplifier was connected to record the thermovoltage directly. After a period of time interval, the voltage amplifier would be cut off while the current amplifier is switched back to measure the conductance again. During the experiment, the tip withdrew from the sample until the tunneling current decreased to achieve the given threshold value. For further details, see section S3 in SI.

### Computational methods

The optimized geometry and ground state Hamiltonian and overlap matrix elements of each structure were self-consistently obtained using the SIESTA implementation of density functional theory (DFT) [39]. SIESTA employs norm-conserving pseudo-potentials to account for the core electrons and linear combinations of atomic orbitals to construct the valence states. The generalized gradient approximation (GGA) of the exchange and correlation functional is used with the Perdew-Burke-Ernzerh of parameterization (PBE), a double- $\zeta$  polarized (DZP) basis set, a real-space grid defined with an equivalent energy cut-off of 200 Ry [49]. The geometry optimization for each structure is performed to the forces smaller than 10 meV/Ang.

The mean-field Hamiltonian obtained from the converged DFT calculation was combined with our home-made implementation of the non-equilibrium Green's function method, Gollum [40], to calculate the phase-coherent, elastic scattering properties of each system consisting of left gold (source) and right gold (drain) leads and the scattering region (molecule **F-DPP**, **T-DPP** and **Thia-DPP**). The transmission coefficient  $T(E)$  for electrons of energy  $E$  (passing from the source to the drain) is calculated via the relation:

$$T(E) = \text{Trace} (\Gamma_R(E)G^R(E)\Gamma_L(E)G^{R\dagger}(E)) \quad (1)$$

In this expression,  $\Gamma_{L,R}(E) = i(\Sigma_{L,R}(E) - \Sigma_{L,R}^\dagger(E))$  describe the level broadening due to the coupling between left (L) and right (R) electrodes and the central scattering region,  $\Sigma_{L,R}(E)$  are the retarded self-energies associated with this coupling and  $G^R(E) = (ES - H - \Sigma_L - \Sigma_R)^{-1}$  is the retarded Green's function, where  $H$  is the Hamiltonian and  $S$  is the overlap matrix. Using the obtained transmission coefficient  $T(E)$ , the electrical conductance  $G(T)$  and the Seebeck coefficient  $S(T)$  can be calculated through the following formula:

$$G = G_0 L_0 \quad (2)$$

$$S = -\frac{L_0}{eTL_1} \quad (3)$$

In the linear response, the quantity of Lorenz number  $L_n(T, E_F)$  is giving by

$$L_n(T, E_F) = \int_{-\infty}^{+\infty} dE (E - E_F)^n T(E) \quad (4)$$

where  $G_0 = 2e^2/h$  is conductance quantum,  $e$  is the charge of a proton;  $h$  is the Planck's constant;  $E_F$  is the Fermi energy;  $f(E) = (1 + \exp((E - E_F)/k_B T))^{-1}$  is the Fermi-Dirac distribution function,  $T$  is the temperature, and  $k_B = 8.6 \times 10^{-5}$  eV/K is Boltzmann's constant.

## Acknowledgments

R.A. and Q.W. would acknowledge the discussions with Dr. Iain Grace for the calculations. C.F., Q.C. and H.C. would acknowledge Dr. Pengcheng Xu for the help of resonant microcantilever thermodynamic desorption characterization and Dr. Lina Chen for the help of X-ray photoelectron spectroscopy characterization.

## Funding

This work was supported by the National Natural Science Foundation of China (No. 21722305, 21933012, 31871877), the National Key R&D Program of China (2017YFA0204902), Natural Science Foundation of Fujian Province (2018J06004), the Beijing National Laboratory for Molecular Sciences (BNLMS202010 and BNLMS202005) and the Fundamental Research Funds for the Central Universities (20720220020, 20720220072, 20720200068, 20720190002). The work in the UK is also supported by the Engineering and Physical Sciences Research Council (EPSRC) through grant nos. EP/M014452/1, EP/P027156/1, and EP/N03337X/1 by the European Commission, the Future and Emerging Technologies (FET) Open project 767187-QuIET and the European (EU) project Bac-to-Fuel.

## Author contributions

W.H. conceived the concept. W.H., C.J.L. and Z.L. co-supervised the project. STM-BJ setup was constructed by H.C. and G.L. in W.H.'s group. H.C. and W.C. carried out single-molecule conductance and thermoelectric experiments. C.F. and H.C. analyzed the experimental data. R.A., Q.W. and S.H. performed theoretical simulations. Z.L. completed the synthesis of molecules used in this work. Y.G., H.Z., Y.Z., J.Z. and B.M. helped to analyze the data. C.F., Q.W., H.C., J. L., Z. L., C.J.L. and W.H. prepared the manuscript. All authors approved the final version of the manuscript.

## Conflict of interest

The authors declare that they have no conflict of interest.

## Data availability

The original data are available from corresponding authors upon reasonable request.

## References

- 1 Wang Y, Yang L, Shi X-L, *et al.* Flexible thermoelectric materials and generators: Challenges and innovations. *Adv Mater* 2019; **31**: 1807916
- 2 Xu K, Sun H, Ruoko T-P, *et al.* Ground-state electron transfer in all-polymer donor–acceptor heterojunctions. *Nat Mater* 2020; **19**: 738-744
- 3 Liang Z, Zhang Y, Souri M, *et al.* Influence of dopant size and electron affinity on the electrical conductivity and thermoelectric properties of a series of conjugated polymers. *J Mater Chem A* 2018; **6**: 16495-16505
- 4 Zeng Y-J, Wu D, Cao X-H, *et al.* Nanoscale organic thermoelectric materials: Measurement, theoretical models, and optimization strategies. *Adv Funct Mater* 2020; **30**: 1903873
- 5 Kim HS, Liu W, Chen G, *et al.* Relationship between thermoelectric figure of merit and energy conversion efficiency. *Proc Natl Acad Sci USA* 2015; **112**: 8205-8210
- 6 Shuai Z, Geng H, Xu W, *et al.* From charge transport parameters to charge mobility in organic semiconductors through multiscale simulation. *Chem Soc Rev* 2014; **43**: 2662-2679
- 7 Zhang Q, Sun Y, Xu W, *et al.* Organic thermoelectric materials: Emerging green energy materials converting heat to electricity directly and efficiently. *Appl Phys Lett* 2014; **26**: 6829-6851
- 8 Huang D, Yao H, Cui Y, *et al.* Conjugated-backbone effect of organic small molecules for n-type thermoelectric materials with  $zT$  over 0.2. *J Am Chem Soc* 2017; **139**: 13013-13023
- 9 Russ B, Glaudell A, Urban JJ, *et al.* Organic thermoelectric materials for energy harvesting and temperature control. *Nat Rev Mater* 2016; **1**: 16050
- 10 Cao X-H, Zhou W-X, Chen C-Y, *et al.* Excellent thermoelectric properties induced by different contact geometries in phenalenyl-based single-molecule devices. *Sci Rep* 2017; **7**: 10842
- 11 Reddy P, Jang S-Y, Segalman RA, *et al.* Thermoelectricity in molecular junctions. *Science* 2007; **315**: 1568-1571
- 12 Kiršanskas G, Li Q, Flensberg K, *et al.* Designing  $\pi$ -stacked molecular structures to control heat transport through molecular junctions. *Appl Phys Lett* 2014; **105**: 233102
- 13 Finch CM, Garca-Suarez VM, Lambert CJ. Giant thermopower and figure of merit in single-molecule devices. *Phys Rev B* 2009; **79**: 033405
- 14 Zeier WG, Zevalkink A, Gibbs ZM, *et al.* Thinking like a chemist: Intuition in thermoelectric materials. *Angew Chem Int Ed* 2016; **55**: 6826-6841
- 15 Li Y, Xiang L, Palma JL, *et al.* Thermoelectric effect and its dependence on molecular length and sequence in single DNA molecules. *Nat Commun* 2016; **7**: 11294
- 16 Dell EJ, Capozzi B, Xia J, *et al.* Molecular length dictates the nature of charge carriers in single-molecule junctions of oxidized oligothiophenes. *Nat Chem* 2015; **7**: 209-214
- 17 Gehring P, Thijssen JM, van der Zant HSJ. Single-molecule quantum-transport phenomena in break junctions. *Nat Rev Phys* 2019; **1**: 381-396
- 18 Aiba A, Demir F, Kaneko S, *et al.* Controlling the thermoelectric effect by mechanical manipulation of the electron's quantum phase in atomic junctions. *Sci Rep* 2017; **7**: 7949
- 19 Garner MH, Koerstz M, Jensen JH, *et al.* Substituent control of  $\sigma$ -interference effects in the transmission of saturated molecules. *ACS Phy Chem Au* 2022; **2**: 282-288
- 20 Miao R, Xu H, Skripnik M, *et al.* Influence of quantum interference on the thermoelectric properties of molecular junctions. *Nano Lett* 2018; **18**: 5666-5672
- 21 Yee SK, Malen JA, Majumdar A, *et al.* Thermoelectricity in fullerene–metal heterojunctions. *Nano Lett* 2011; **11**: 4089-4094
- 22 Widawsky JR, Darancet P, Neaton JB, *et al.* Simultaneous determination of conductance and thermopower of single molecule junctions. *Nano Lett* 2012; **12**: 354-358
- 23 Baheti K, Malen JA, Doak P, *et al.* Probing the chemistry of molecular heterojunctions using thermoelectricity. *Nano Lett* 2008; **8**: 715-719

- 24 Li X, Wu Q, Bai J, *et al.* Structure-independent conductance of thiophene-based single-stacking junctions. *Angew Chem Int Ed* 2020; **59**: 3280-3286
- 25 Evangelini C, Gillemot K, Leary E, *et al.* Engineering the thermopower of c60 molecular junctions. *Nano Lett* 2013; **13**: 2141-2145
- 26 Imahori H, Hasobe T, Yamada H, *et al.* Concentration effects of porphyrin monolayers on the structure and photoelectrochemical properties of mixed self-assembled monolayers of porphyrin and alkanethiol on gold electrodes. *Langmuir* 2001; **17**: 4925-4931
- 27 Nerngchamnong N, Yuan L, Qi D-C, *et al.* The role of van der waals forces in the performance of molecular diodes. *Nat Nanotechnol* 2013; **8**: 113-118
- 28 Romaner L, Heimel G, Zojer E. Electronic structure of thiol-bonded self-assembled monolayers: Impact of coverage. *Phys Rev B* 2008; **77**: 045113
- 29 Song H, Lee H, Lee T. Intermolecular chain-to-chain tunneling in metal–alkanethiol–metal junctions. *J Am Chem Soc* 2007; **129**: 3806-3807
- 30 Jalal Uddin M, Khalid Hossain M, Hossain MI, *et al.* Modeling of self-assembled monolayers (sams) of octadecanethiol and hexadecanethiol on gold (au) and silver (ag). *Results Phys* 2017; **7**: 2289-2295
- 31 Chen H, Sangtarash S, Li G, *et al.* Exploring the thermoelectric properties of oligo(phenylene-ethynylene) derivatives. *Nanoscale* 2020; **12**: 15150-15156
- 32 Xu B, Tao NJ. Measurement of single-molecule resistance by repeated formation of molecular junctions. *Science* 2003; **301**: 1221-1223
- 33 Shi L, Majumdar A. Thermal transport mechanisms at nanoscale point contacts. *J Heat Transfer* 2001; **124**: 329-337
- 34 Grant JT. Methods for quantitative analysis in xps and aes. *Surf Interface Anal* 1989; **14**: 271-283
- 35 Suroviec A. Determining surface coverage of self-assembled monolayers on gold electrodes. *Chem Educator* 2012; **17**: 83
- 36 Bard A, Faulkner L, *Electrochemical methods – fundamentals and applications*. John Wiley & Sons, Ltd., New York, 1981.
- 37 Yu H, Li X, Gan X, *et al.* Resonant-cantilever bio/chemical sensors with an integrated heater for both resonance exciting optimization and sensing repeatability enhancement. *J Micromech Microeng* 2009; **19**: 045023
- 38 Paulsson M, Datta S. Thermoelectric effect in molecular electronics. *Phys Rev B* 2003; **67**: 241403
- 39 Soler J, Artacho E, Gale J, *et al.* The siesta method for ab initio order-n materials simulation. *J Phys Condens Matter* 2002; **14**:
- 40 Ferrer J, Lambert C, Garc ía-Su árez V, *et al.* Gollum: A next-generation simulation tool for electron, thermal and spin transport. *New J Phys* 2014; **16**: 093029
- 41 Kashimoto Y, Yonezawa K, Meissner M, *et al.* The evolution of intermolecular energy bands of occupied and unoccupied molecular states in organic thin films. *J Phys Chem C* 2018; **122**: 12090-12097
- 42 Lambert CJ. Basic concepts of quantum interference and electron transport in single-molecule electronics. *Chem Soc Rev* 2015; **44**: 875-888
- 43 Wang X, Jiang B, Du C, *et al.* Fluorinated dithienyl-diketopyrrolopyrrole: A new building block for organic optoelectronic materials. *New J Chem* 2019; **43**: 16411-16420
- 44 Neaton JB, Hybertsen MS, Louie SG. Renormalization of molecular electronic levels at metal-molecule interfaces. *Physical Review Letters* 2006; **97**: 216405
- 45 Mueller CJ, Singh CR, Fried M, *et al.* High bulk electron mobility diketopyrrolopyrrole copolymers with perfluorothiophene. *Adv Funct* 2015; **25**: 2725-2736
- 46 Sonar P, Zhuo J-M, Zhao L-H, *et al.* Furan substituted diketopyrrolopyrrole and thienylenevinylene based low band gap copolymer for high mobility organic thin film transistors. *J Mater* 2012; **22**: 17284-17292
- 47 Carsten B, Szarko JM, Lu L, *et al.* Mediating solar cell performance by controlling the internal dipole change in organic photovoltaic polymers. *Macromolecules* 2012; **45**: 6390-6395
- 48 Haiss W, van Zalinge H, Higgins SJ, *et al.* Redox state dependence of single molecule conductivity. *J Am Chem Soc* 2003; **125**: 15294-15295
- 49 Perdew JP, Burke K, Ernzerhof M. Perdew, burke, and ernzerhof reply. *Phys Rev Lett* 1998; **80**: 891-891

## Supporting Information for:

# Intermolecular Coupling Enhanced Thermopower in Single-Molecule Diketopyrrolopyrrole Junctions

Chao Fang<sup>1,#</sup>, Renad Almughathawi<sup>2,6,#</sup>, Qingqing Wu<sup>2,#</sup>, Wenqiang Cao<sup>1,#</sup>, Hang Chen<sup>1,#</sup>, Songjun Hou<sup>2</sup>, Yu Gu<sup>1</sup>, Hewei Zhang<sup>1</sup>, Yi Zhao<sup>1</sup>, Jueting Zheng<sup>1</sup>, Guopeng Li<sup>1</sup>, Jia Shi<sup>1</sup>, Junyang Liu<sup>1,4</sup>, Bing-Wei Mao<sup>1</sup>, Zitong Liu<sup>3,5,\*</sup>, Colin J. Lambert<sup>2,\*</sup>, Wenjing Hong<sup>1,4,5,\*</sup>

<sup>1</sup>State Key Laboratory of Physical Chemistry of Solid Surfaces, College of Chemistry and Chemical Engineering, Xiamen University, Xiamen 361005, China.

<sup>2</sup>Department of Physics, Lancaster University, LA1 4YB, Lancaster, UK.

<sup>3</sup>State Key Laboratory of Applied Organic Chemistry (SKLAOC), College of Chemistry and Chemical Engineering, Lanzhou University, Lanzhou, 730000, P. R. China.

<sup>4</sup>Innovation Laboratory for Sciences and Technologies of Energy Materials of Fujian Province (IKKEM), Xiamen 361005, China

<sup>5</sup>Beijing National Laboratory for Molecular Sciences, 100190 Beijing, P. R. China.

<sup>6</sup>Department of physics, Faculty of Science, Taibah University, Madinah, Saudi Arabia.

#Contributed equally to this work.

\*E-mail: liuzt@lzu.edu.cn; c.lambert@lancaster.ac.uk; whong@xmu.edu.cn

## Content

1. Synthesis Information.....	2
2. Experimental technique.....	2
2.1 Preparation of STM tips and Au substrate .....	2
2.2 Monolayer characterization .....	2
2.2.1 Electrochemical cyclic voltammetry .....	2
2.2.2 X-ray photoelectron spectroscopy .....	4
2.2.3 Micro thermal gravimetric analyzer .....	5
2.3 Data analysis.....	6
3. Single-molecule conductance and Seebeck coefficient measurement .....	6
4. Theoretical calculation .....	11
Reference .....	16

## 1. Synthesis Information

The reagents and starting materials including compound M1 (Figure. S1) were commercially available and used without any further purification, if not specified elsewhere. Compound M2 and M3 (Figure. S1) were synthesized according to the previous report [1-4].

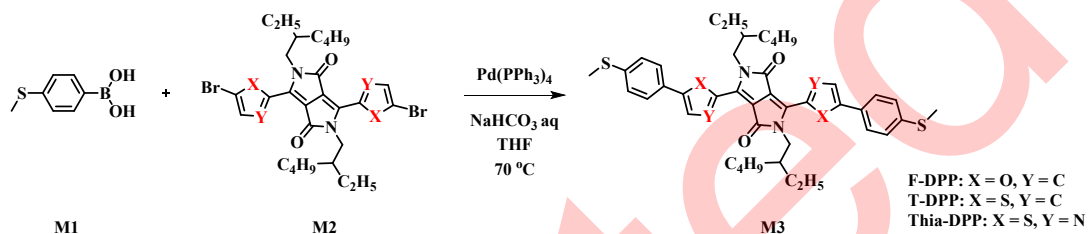


Figure S1. Synthetic routes to three DPP derivatives.

## 2. Experimental Technique

### 2.1 Preparation of STM tips and SAMs

We used the electrochemical etching method to prepare the STM tips. A mixed solution of concentrated hydrochloric solution (containing 37% HCl) and ethanol with a proportion of 1:1 in volume was prepared. A gold ring was immersed below the solution surface with a 3/4 height. A 0.25 mm diameter gold wire (99.99%, Jiaming, Beijing) was prepared and immersed in the solution at the center of the gold ring. The wire was electrochemically etched until severed, then the etching stopped. The etched gold tip was rinsed by isopropanol thoroughly and dried by N<sub>2</sub> gas before further usage.

To obtain SAMs with different packing densities, the gold substrates, which are prepared by coating 200 nm Au film on silicon wafers, were immersed into 0.01mM, 0.1mM, 1 mM molecule solutions respectively using 1,2,4-trichlorobenzene (TCB, 99.9%, Sigma Aldrich) as solvent for 4 hours. Then, rinse the SAMs with the TCB for 1 minute to remove the surface molecules by physical absorption, followed by N<sub>2</sub> gas drying. Besides, it is difficult to assemble monolayers if we continued to increase the immersion concentration, because the molecules would tend to aggregate on the surface of substrate instead of forming a SAM, resulting in no signals of molecular conductance during STM-BJ measurement.

## 2.2 Monolayer Characterization

### 2.2.1 Electrochemical cyclic voltammetry

The SAMs of **F-DPP** on Au electrodes were electrochemically characterized by cyclic voltammetry (CV). To perform the CV measurements, we used an electrochemical cell placed in a Faraday cage equipped with platinum counter as electrode, standard calomel as reference electrode and gold with **F-DPP** assembled on as a working electrode. The preparation of the gold electrode is same with the SAMs used for STM. Cyclic voltammetry was recorded in 2.5 mM K<sub>3</sub>Fe(CN)<sub>6</sub>/K<sub>4</sub>Fe(CN)<sub>6</sub> containing 0.1 M KNO<sub>3</sub> as the supporting electrolyte between -0.2 to 0.6 V at a scan rate of 100 mV/s. Within this potential range, redox reaction between K<sub>3</sub>Fe(CN)<sub>6</sub> and K<sub>4</sub>Fe(CN)<sub>6</sub> took place, and there were no other redox reactions from the SAMs.

The gold electrode surface with **F-DPP** assembled on would occupy the sites of redox reaction and stop reactants diffusing in and participating in reaction. The surface area without **F-DPP** assembled on can be reflected by diffusion area, which could be obtained from Cottrell equation [5]:

$$i = \frac{nFAc_0D^{0.5}}{\pi^{0.5}t^{0.5}} \quad (1)$$

Where  $i$  is the current decided by diffusion,  $n$  is the number of electrons transfer per reaction (1 in this work),  $F$  is the Faraday constant (96485 C/mol),  $A$  is the area of reactants diffusion,  $C_0$  is the

initial concentration of reactant (2.5 mM),  $D$  is the diffusion constant of  $K_3Fe(CN)_6$  in electrolyte ( $7.6 \times 10^{-6} \text{ cm}^2/\text{s}$ ) [6],  $t$  is the time. Integrating the Cottrell equation:

$$Q = \frac{2nFAC_0D^{0.5}t^{0.5}}{\pi^{0.5}} \quad (2)$$

Where  $Q$  is the total transferred charge. Taking the gold electrode without **F-DPP** assembled on as an example (the black curve in Figure 2a of the main text), we picked the potential at the oxidation peak (0.218V) as the beginning of diffusion, where diffusion starts to dominant the current. Therefore, a graph of transferred charge vs. square root of time could be obtained (Figure S2).

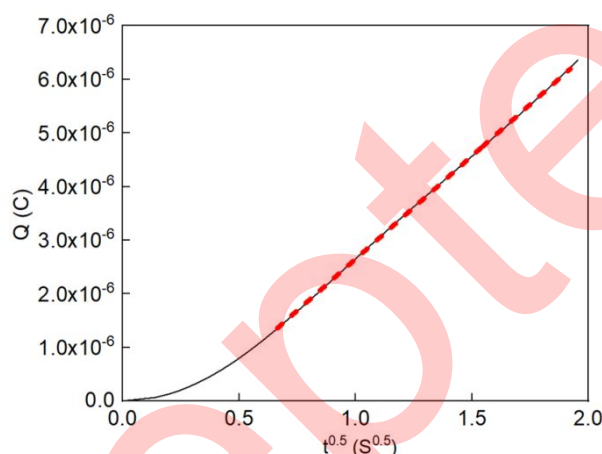


**Figure S2.** Transferred charge vs. square root of time in the diffusion-dominated CV area with bare gold as working electrode. The red dashed line indicates the linear fitting.

According to Equation (2), the slope of linear fitting in Figure S2 is proportional to the diffusion area, which can be roughly estimated to be  $0.0051 \text{ cm}^2$  for the bare gold electrode. By this way, diffusion area of the gold electrode with different **F-DPP** immersion concentrations could all be determined (See Table 1 in main text). There are differences between the estimated diffusion area and actual area exposed to the electrolyte solution (2 mm diameter) for bare gold, this is because it's not a pure diffusion process, and the initial concentration and diffusion constant are not absolutely accurate. The fraction of surface coverage by SAM can be obtained from Equation (3):

$$F = \left(1 - \frac{S_d}{S_{bare}}\right) * 100\% \quad (3)$$

Where  $S_d$  is the diffusion area obtained from Cottrell equation for gold electrode with molecules assembled on,  $S_{bare}$  is the diffusion area for the bare gold electrode.

### 2.2.2 X-ray photoelectron spectroscopy

X-ray photoelectron spectroscopy (XPS) was used to characterize the SAMs to determine the chemical composition and atomic percentage [7]. The measurements were performed at the ESCALAB 250Xi system (Thermo Fisher Scientific). Spectra were collected using a

monochromatic Al X-ray source (Al K $\alpha$  1486.6 eV). The spectra were fitted by symmetric Voigt functions and a linear or Shirley-type background. The S 2p doublet was fitted by two peaks with the same full width at half-maximum (FWHM), the standard spin-orbit splitting of 1.2 eV, and the branching ratio of S 2p $_{3/2}$  / S 2p $_{1/2}$  is 2 [8].

The Au 4f $_{7/2}$  and S 2p spectra of the SAMs are presented in Figure S3. The Au 4f $_{7/2}$  spectra of all SAMs exhibit similar intensity of the Au 4f $_{7/2}$  peak, which means a similar effective thickness of all these monolayers. The S 2p spectra can be decomposed into individual contributions (S 2p $_{3/2, 1/2}$  doublets) associated with specific sulfur-containing groups in the SAM. The S 2p spectra exhibit the characteristic signals of the formation of a gold-thiolate bond (1) at ca. 162.5 eV (S 2p $_{3/2}$ ). However, the higher binding peak at ~ 163-164 eV has alternatively been attributed to unbound -SAc group (2). The ratio of atomic concentration of S was obtained by Equation (4):

$$\frac{n_S}{n_{Au}} = \frac{I_S/S_S}{I_{Au}/S_{Au}} \quad (4)$$

Where  $n$  is the concentration of an atom,  $I$  is the integrated peak area,  $S$  is the atomic sensitivity factor [9, 10]. The XPS data indicated that more molecules existed on the gold sample with increasing immersion concentrations based on the atomic concentration of the S 2p peak signal.

**Table S1.** The atomic concentration of S in the **F-DPP** SAMs with three different immersion concentrations determined by XPS

Structures	0.01 mM F-DPP	0.1 mM F-DPP	1 mM F-DPP
The atomic concentration of S (%)	2.1	3.29	3.61

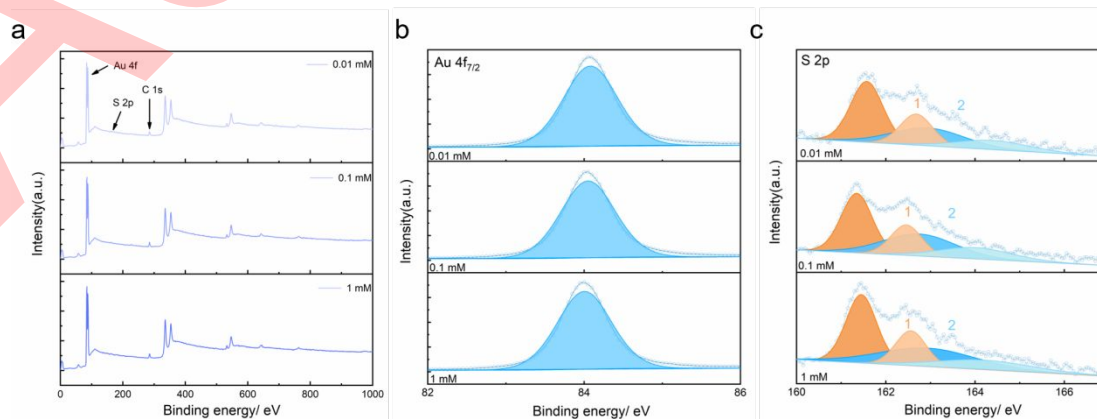


**Figure S3.** a) The panels (from top to bottom) indicated a wide-scan spectra of gold samples coated with 0.01 mM to 1 mM **F-DPP** monolayers. b) From top to bottom: The Au 4f spectra of 0.01 mM

to 1 mM **F-DPP** monolayers. c) The panels (from top to bottom) indicated the S 2p spectra of corresponding gold surface composition. The S 2p spectra can be decomposed into individual contributions (S 2p<sub>3/2</sub>, 1/2 doublets): Au-S bond (1, orange) and unbound S (2, blue).

### 2.2.3 Micro thermal gravimetric analyzer

Micro thermal gravimetric analyzer ( $\mu$ -TGA) was used to characterize the molecular mass of self-assembled monolayers by resonant micro-cantilever gravimetric sensing experiment [11]. By using the  $\mu$ -TGA method, mass change results from sample decomposition can be quantitatively measured. After the same amount of molecular solution was adsorbed at the surface of the cantilever, a small mass was desorbed at the surface of the cantilever with the increasing temperature. The resonant micro-cantilever is considered to be a microgravimetric sensor, using mass-desorption-induced resonant frequency shift as a sensing signal (Figure. S4a) [12]. 1 mM **F-DPP** SAMs lead to a 351 Hz frequency shift, and 0.1mM **F-DPP** leads to a 182 Hz shift. The frequency shift was not clear in the 0.01 mM **F-DPP**, and it means that the molecules were too little to be detected (Figure. S4b). It can be seen that more molecules existed on the gold sample with increasing concentrations.

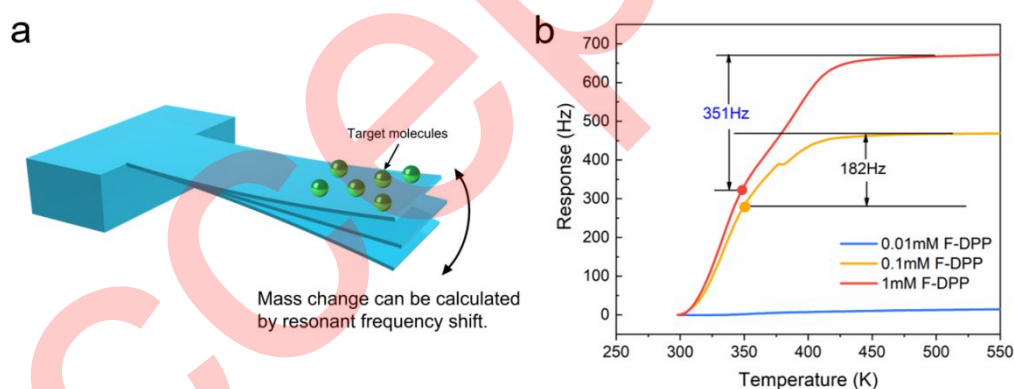


**Figure S4.** a) schematic diagram of micro thermal gravimetric analyzer. b) The frequency shift curves are extracted from different concentration **F-DPP** molecule gravimetric desorption experiments at different temperatures using a resonant cantilever. The red and orange circles mean the turning point that the desorption change from physical adsorption molecules to chemical adsorption molecules.

### 2.2.4 Data analysis

All thermoelectric data (Figure 1 and Figure 2) in the main manuscript and the supporting information (Figure S7) were plotted in Origin. The peak values in the histograms, corresponding to the Gaussian fit, provided the most probable thermoelectric voltage value in the corresponding temperature difference. The standard error was used to show the uncertainty of thermoelectric voltage. The thermoelectric voltage can be expressed as a function of  $\Delta T$ . The Seebeck coefficients

were obtained from the slope by the linear fitting and the standard error associated with the slope. The same approaches were used to process the data from all thermoelectric experiments.

### **3. Single-molecule Conductance and Seebeck Coefficient Measurement**

Accepted

The etched gold tip was used to contact the molecule, and the STM-BJ measurements were performed in soft-contact mode at room temperature [13]. The soft-contact measurement can prevent contact between the tip and the substrate to avoid direct heat transfer during the thermoelectric experiment. A fixed bias voltage of 0.1 V was added between the tip and the substrate. The tip, controlled by the motor and piezoelectric actuator, withdrew from the sample until the increase of tunneling current achieves the given threshold value. A threshold conductance value  $0.01G_0$  (where  $G_0$  is the quantum conductance, which equals  $2e^2/h$ ) was chosen to indicate the formation of the single-molecule junction and prevent the Au STM tip from bringing into contact with the Au substrate. Spontaneous formation of stable molecular junctions was observed. More than 2000 individual conductance-distance traces without any selection were recorded for each molecule for further statistical analysis. To find the most probable conductance value for each molecule, one-dimensional (1D) conductance histograms constructed from 2000 conductance-distance traces without any selection were plotted in Figure S5a for F-DPP. The peaks were identified in the histogram, and single-molecule conductance plateaus of F-DPP vary from  $10^{-4.02}G_0$  (0.1 mM) to  $10^{-3.93}G_0$  (1 mM) that suggests the conductance increases slightly with increasing the packing density. The plateaus and peaks were further verified by a clear molecular density cloud in the corresponding two-dimensional (2D) conductance-distance histograms as showed in Figure S5b-c. The conductance data for T-DPP and Thia-DPP was shown in Figure S6, and all conductance data were summarized in Table 2 of the main text. It can be seen that conductance increases slightly with increasing the molecular packing density and the intermolecular gating effect on the charge transport is less obvious. However, single-molecule conductance plateaus of three molecules reduce gradually from F-DPP to Thia-DPP. All results show that the single-molecule conductance can be tuned by altering the adjacent aromatic rings of the DPP core.

To determine the stretching distance distributions, we correct the speed of piezo by the tunnelling region between  $10^{-3}G_0$  to  $10^{-5}G_0$  based on those traces without conductance plateau (without forming molecular junction). The distance for the stretching from  $10^{-3}G_0$  to  $10^{-5}G_0$  should be 0.36 nm, as reported previously [14, 15]. Thus, we could precisely know the speed of piezo to determine the junction lengths.

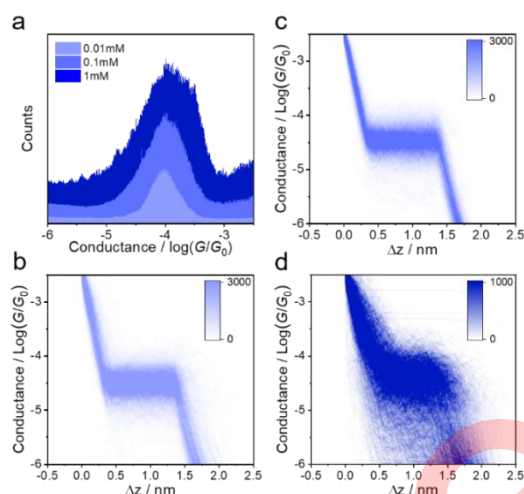


**Figure S5.** Single-molecule conductance results from soft-contact STM-BJ experiments. a) 1D conductance histograms constructed from 2000 conductance-distance traces without any selection for 0.01, 0.1, 1mM **F-DPP**. b-d) 2D conductance histograms for 0.01, 0.1, 1mM **F-DPP**, respectively.

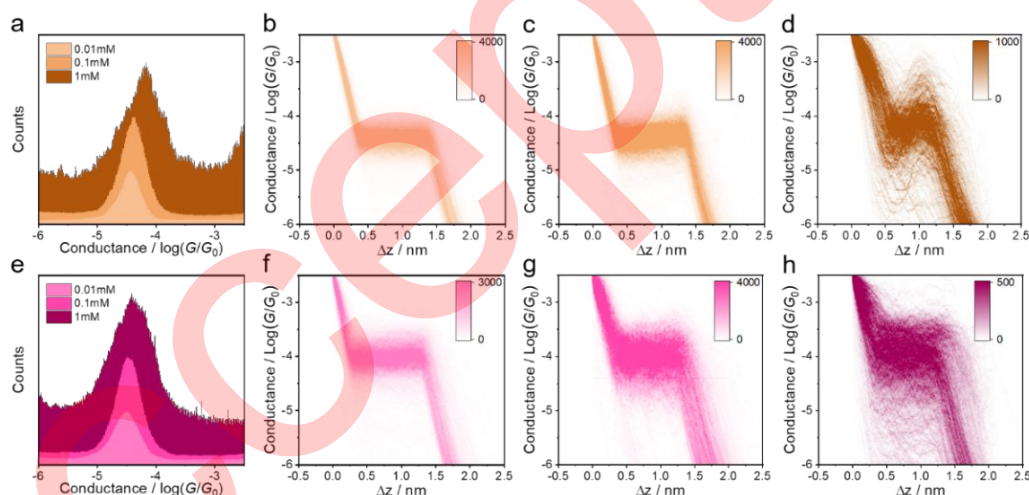


**Figure S6.** a) 1D conductance histograms constructed from 2000 conductance-distance traces without any selection for 0.01, 0.1, 1mM **T-DPP**. b-d) 2D conductance histograms for 0.01, 0.1, 1mM **T-DPP**, respectively. e) 1D conductance histograms constructed from 2000 conductance-distance traces without any selection for 0.01, 0.1, 1mM **Thia-DPP**. f-h) 2D conductance histograms for 0.01, 0.1, 1mM **Thia-DPP**, respectively.

The whole thermoelectric measurement process was shown in Figure S7. When the conductance plateau was first detected, the bias would be switched from 0.1 V to 0.2 V and held for 50 ms. The conductance value under 0.2 V bias during the 50 ms was analyzed further. If the conductance values were the same as the measured value under 0.1 V bias, the tip would be hovered and fixed the tip/substrate distance. Once the tip has successfully hovered, the current amplifier will be cut off with the bias voltage switched to 0 V. The voltage amplifier is connected to start the thermoelectricity mode by a relay control. The thermovoltage is recorded directly by a differential-

input voltage amplifier with 100 times amplification factor during the middle 100 ms of the 200 ms period when the tip/substrate distance is fixed (green area in Figure S7). Then, the voltage amplifier would be cut off, and the bias would be switched back to 0.2 V again, fixed for 50 ms to measure the conductance at that time. Briefly, the single-molecule junction conductance during the first and last 50 ms of the “hold” period is confirmed. If both measured conductance at this time were found to be within a molecule-dependent range from conductance histogram, we consider that the molecular junction was stable during the entire thermoelectric measurement, and all the thermovoltage data come from the single-molecule junctions. Finally, the bias would be recovered to 0.1 V. The tip withdrew from the sample until the tunneling current decreases to achieve the given threshold value. Thus, the measurement continued to repeat the steps above for the next cycle. The thermopower of the molecular junction is given by Equation 5 [13, 16]:

$$\Delta S_{junction} = \Delta S_{Au} - \frac{\Delta V_{th}}{\Delta T} \quad (5)$$

Where  $S_{Cu}$  (1.94  $\mu\text{V}/\text{K}$ ) is the Seebeck coefficient of bulk gold at  $T = 300 \text{ K}$ .

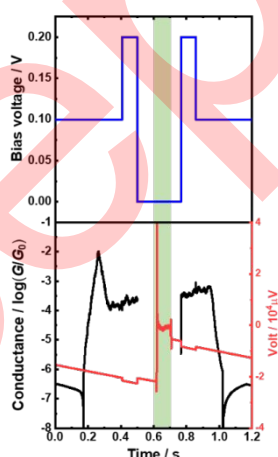


**Figure S7.** Typical thermoelectric measurement process. The panels (from top to bottom) indicate bias voltage, measured conductance, and thermovoltage of the molecule as a function of time. The green area indicates the actual thermovoltage measurement period.

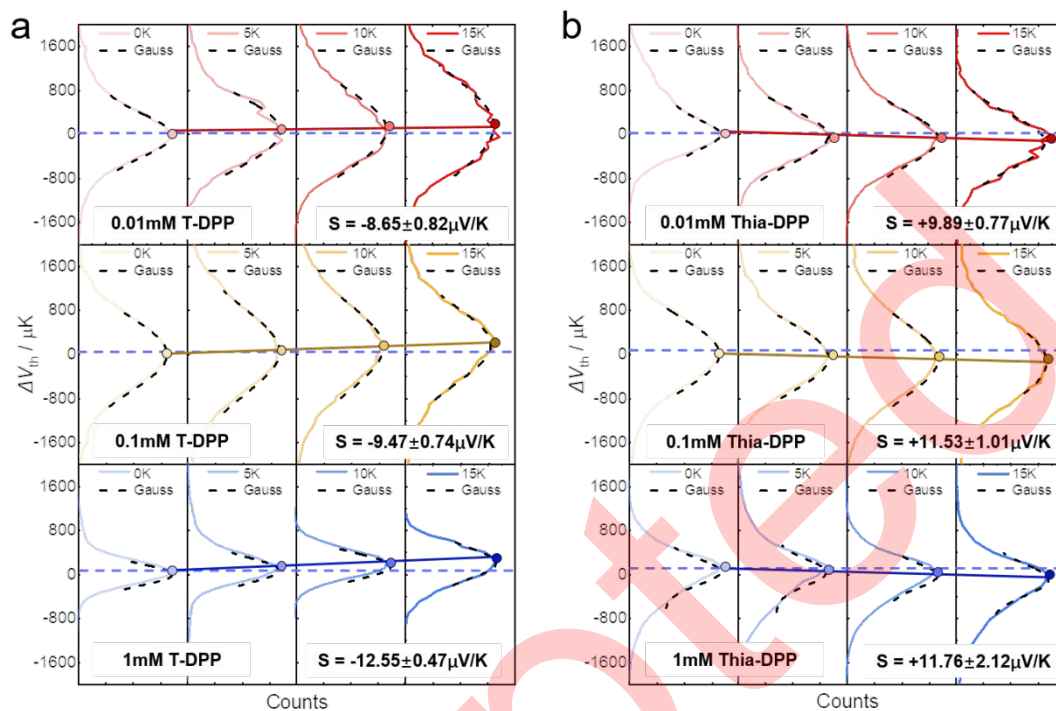


**Figure S8.** Measured Seebeck coefficient value for **T-DPP** and **Thia-DPP**. a) Histograms of 0.01, 0.1, 1 mM **T-DPP** thermoelectric voltage measurements at a series of  $\Delta T = 0$  K, 5 K, 10 K, and 15 K, respectively. Gaussian fits plotted in black short dash line. The black dash line indicates the baseline of thermoelectric voltage at  $\Delta V_{th} = 0$ . The Seebeck coefficients were obtained from the thermovoltage as a function of  $\Delta T$ . Solid lines are linear fitting. b) Histograms of **Thia-DPP** thermoelectric voltage measurements.

#### 4. Theoretical calculation

The optimized geometry and ground state Hamiltonian and overlap matrix elements of each structure were self-consistently obtained using the SIESTA implementation of density functional theory (DFT) [17]. SIESTA employs norm-conserving pseudo-potentials to account for the core electrons and linear combinations of atomic orbitals to construct the valence states. The generalized gradient approximation (GGA) of the exchange and correlation functional is used with the Perdew-Burke-Ernzerhof parameterization (PBE), a double- $\zeta$  polarized (DZP) basis set, a real-space grid defined with an equivalent energy cut-off of 200 Ry [18]. The geometry optimization for each structure is performed to the forces smaller than 10 meV/Ang.

The mean-field Hamiltonian obtained from the converged DFT calculation was combined with our home-made implementation of the non-equilibrium Green's function method, Gollum [19], to calculate the phase-coherent, elastic scattering properties of each system consisting of left gold (source) and right gold (drain) leads and the scattering region (molecule **F-DPP**, **T-DPP**, and **Thia-DPP**). The transmission coefficient  $T(E)$  for electrons of energy  $E$  (passing from the source to

the drain) is calculated via the relation:

$$T(E) = \text{Trace} (\Gamma_R(E)G^R(E)\Gamma_L(E)G^{R\dagger}(E)) \quad (6)$$

In this expression,  $\Gamma_{L,R}(E) = i(\Sigma_{L,R}(E) - \Sigma_{L,R}^\dagger(E))$  describe the level broadening due to the coupling between left (L) and right (R) electrodes and the central scattering region,  $\Sigma_{L,R}(E)$  are the retarded self-energies associated with this coupling and  $G^R(E) = (ES - H - \Sigma_L - \Sigma_R)^{-1}$  is the retarded Green's function, where  $H$  is the Hamiltonian and  $S$  is the overlap matrix. Using the obtained transmission coefficient  $T(E)$ , the electrical conductance  $G(T)$  and the Seebeck coefficient  $S(T)$  can be calculated through the following formula:

$$G = G_0 L_0 \quad (7)$$

$$S = -\frac{L_0}{eTL_1} \quad (8)$$

In the linear response, the quantity of Lorenz number  $L_n(T, E_F)$  is giving by

$$L_n(T, E_F) = \int_{-\infty}^{+\infty} dE (E - E_F)^n T(E) \quad (9)$$

where  $G_0 = 2e^2/h$  is conductance quantum,  $e$  is the charge of a proton;  $h$  is the Planck's constant;  $E_F$  is the Fermi energy;  $f(E) = (1 + \exp((E - E_F)/k_B T))^{-1}$  is the Fermi-Dirac distribution function,  $T$  is the temperature, and  $k_B = 8.6 \times 10^{-5}$  eV/K is Boltzmann's constant.

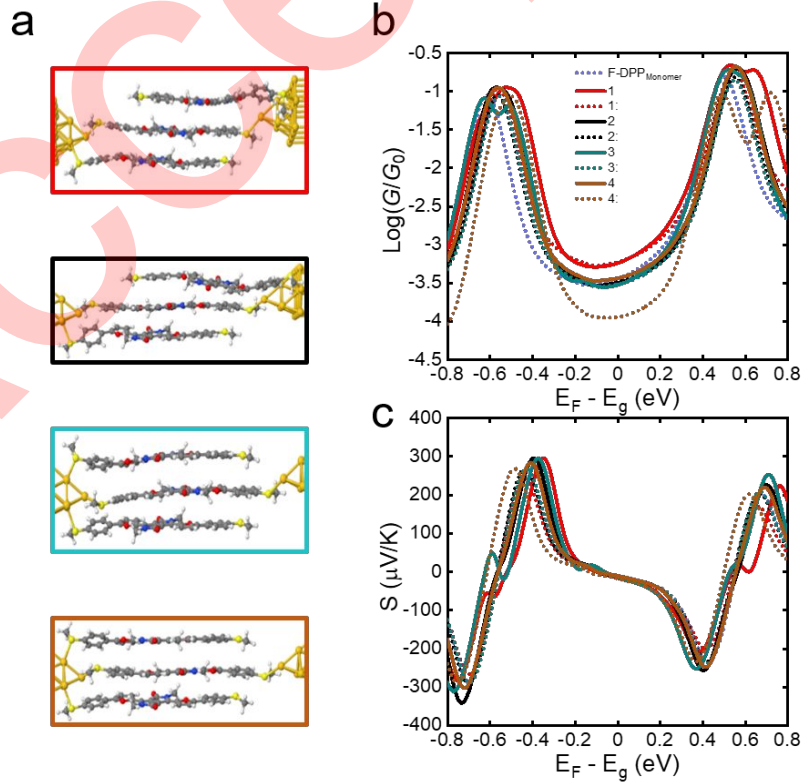


**Figure S9.** DFT-based electrical and thermoelectric properties of the DPP derivatives are attached to gold electrodes via -SMe anchor groups. a) Models for Trimer **F-DPP** with several binding confirmations. b) The corresponding room-temperature electrical conductance as a function of the Fermi energy  $E_F$  relative to the Mid-Gap  $E_g$ . This conductance of each pair of the monomer and trimer is aligned by the mid-gaps, respectively. Dotted curves represent the monomer derivatives, and the trimer derivatives are depicted by solid curves, respectively. c) Seebeck coefficients as a function of Fermi energy  $E_F$  at room temperature 300 K, with the same shifting with the corresponding conductance.

In the same way as the **F-DPP** molecule attached to the electrode with several binding configurations, we sampled other different configurations with three molecules in the junction for **T-DPP** and **Thia-DPP** (Figure S10). The details depend on how these molecules bind, as shown in Figure 3 in the main text.

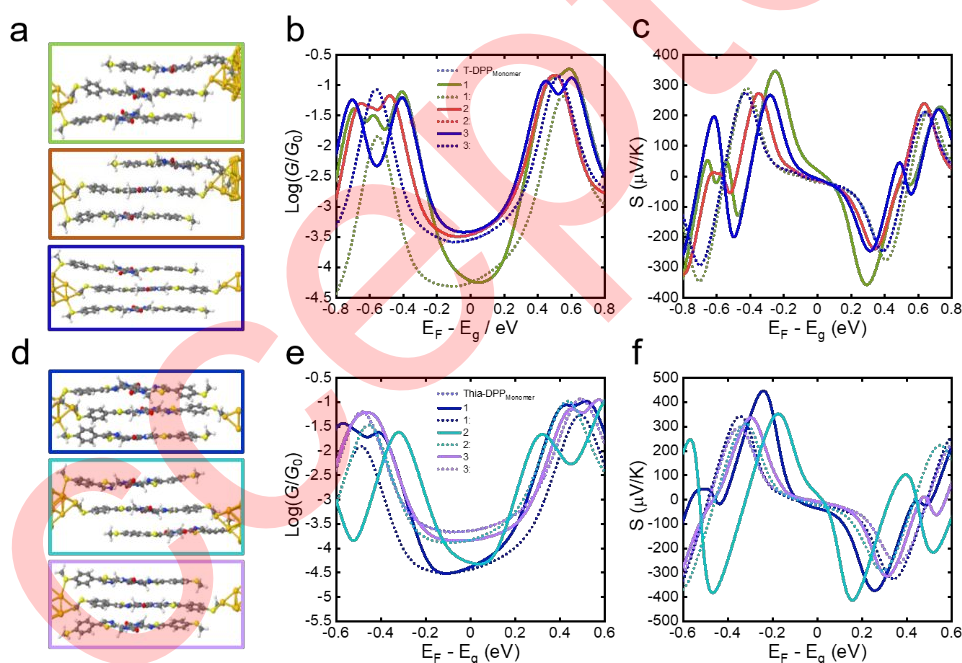


**Figure S10.** DFT-based thermoelectric properties of the **T-DPP** and **Thia-DPP** attached to gold electrodes via -SMe anchor groups. a, d) an example of Trimer **T-DPP** and **Thia-DPP** with several binding configurations. b, e) The corresponding room-temperature electrical conductance as a function of the Fermi energy  $E_F$  relative to the Mid-Gap  $E_g$  of different binding confirmations for **T-DPP** and **Thia-DPP**, respectively. The conductance of each pair of the monomer and trimer are aligned by the mid-gaps. The monomer derivatives are represented by dotted curves, and the trimer derivatives are depicted by solid curves, respectively. c, f) Seebeck coefficients as a function of Fermi energy  $E_F$  at room temperature 300 K, with the same shifting with the corresponding conductance.

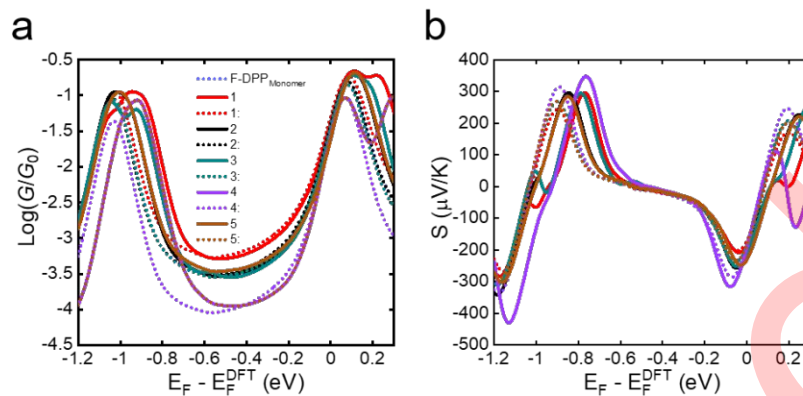


**Figure S11.** DFT-based thermoelectric properties of the **F-DPP** attached to gold electrodes via -SMe anchor groups. (a) The corresponding room-temperature electrical conductance as a function of the Fermi energy  $E_F$  relative to the one predicted by DFT. (b) Seebeck coefficients ( $S$ ) as a function of fermi-energy  $E_F$  at room temperature 300 K. The monomer derivatives are represented by dotted curves, and the trimer derivatives are depicted by solid curves, respectively.

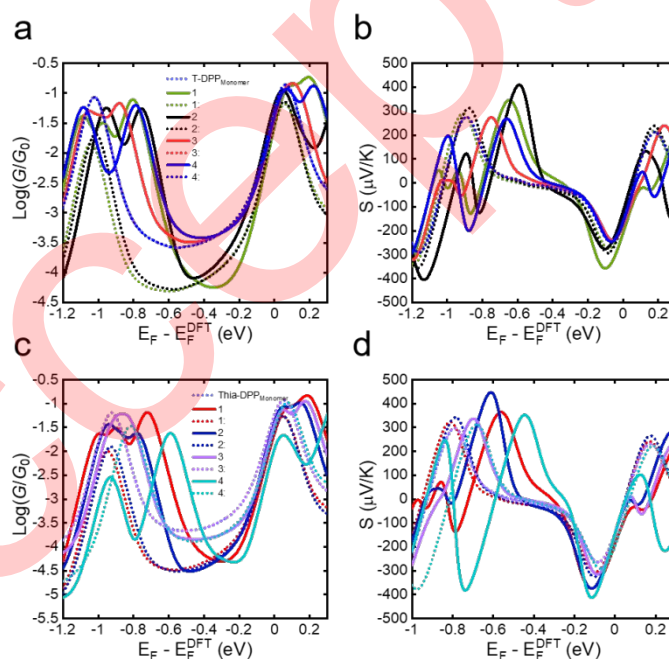


**Figure S12.** DFT-based thermoelectric properties of the **T-DPP** and **Thia-DPP** attached to gold electrodes via -SMe anchor groups. a, c) The corresponding room-temperature electrical conductance as a function of the Fermi energy  $E_F$  relative to the one predicted by DFT. b, d) Seebeck coefficients ( $S$ ) as a function of fermi-energy  $E_F$  at room temperature 300 K. The monomer derivatives are represented by dotted curves, and the trimer derivatives are depicted by solid curves, respectively.

Figures S11 and Figure S12 show DFT results for the electrical conductance, and the Seebeck coefficient is a function of the Fermi energy. Thus, over the energy range between the HOMO-

LUMO gap, we found either the dotted lines of the monomer junctions are close to or below the solid lines of the trimer junctions. Therefore, the qualitative behavior over the range of energies is that the trimer-junction Seebeck coefficients are higher than those of the monomer junctions. To emphasize these trends, we shifted the energy origin to make the Seebeck coefficients pass through zero at the same energy, which means the mid-gap energy of the molecules is aligned. The qualitative trends are maintained, as shown in Figure 3 of the manuscript. Besides, the Table S2 shows that the three molecules attached to the gold gain electron in the junction.

**Table S2.** Voronoi Net Atomic Populations of **F-DPP**, **T-DPP**, and **Thia-DPP**

Structures	Difuranyl-DPP (F-DPP)	Dithienyl-DPP (T-DPP)	Dithiazolyl-DPP (Thia-DPP)
Voronoi of the molecule in the junction	-0.147	-0.153	-0.205

## Reference

- 1 Carsten B, Szarko JM, Lu L, *et al.* Mediating solar cell performance by controlling the internal dipole change in organic photovoltaic polymers. *Macromolecules* 2012; **45**: 6390-6395
- 2 Sonar P, Zhuo J-M, Zhao L-H, *et al.* Furan substituted diketopyrrolopyrrole and thienylenevinylene based low band gap copolymer for high mobility organic thin film transistors. *J Mater* 2012; **22**: 17284-17292
- 3 Mueller CJ, Singh CR, Fried M, *et al.* High bulk electron mobility diketopyrrolopyrrole copolymers with perfluorothiophene. *Adv Funct Mater* 2015; **25**: 2725-2736
- 4 Tan Z, Jiang W, Tang C, *et al.* The control of intramolecular through-bond and through-space coupling in single-molecule junctions. *CCS Chem* 2021; **4**: 713-721
- 5 Bard A, Faulkner L, *Electrochemical methods – fundamentals and applications*. John Wiley & Sons, Ltd., New York, 1981.
- 6 Suroviec A. Determining surface coverage of self-assembled monolayers on gold electrodes. *Chem Educator* 2012; **17**: 83
- 7 Grant JT. Methods for quantitative analysis in xps and aes. *Surf Interface Anal* 1989; **14**: 271-283
- 8 Cavalleri O, Gonella G, Terreni S, *et al.* High resolution xps of the s 2p core level region of the l-cysteine/gold interface. *J Phys Condens* 2004; **16**: S2477-S2482
- 9 Li Z, Lieberman M, Hill W. Xps and sers study of silicon phthalocyanine monolayers: Umbrella vs octopus design strategies for formation of oriented sams. *Langmuir* 2001; **17**: 4887-4894
- 10 Zhong C-J, Brush RC, Andereg J, *et al.* Organosulfur monolayers at gold surfaces: Reexamination of the case for sulfide adsorption and implications to the formation of monolayers from thiols and disulfides. *Langmuir* 1999; **15**: 518-525
- 11 Yu H, Li X, Gan X, *et al.* Resonant-cantilever bio/chemical sensors with an integrated heater for both resonance exciting optimization and sensing repeatability enhancement. *J Micromech Microeng* 2009; **19**: 045023

- 12 Xu P, Yu H, Guo S, *et al.* Microgravimetric thermodynamic modeling for optimization of chemical sensing nanomaterials. *Anal Chem* 2014; **86**: 4178-4187
- 13 Chen H, Sangtarash S, Li G, *et al.* Exploring the thermoelectric properties of oligo(phenylene-ethynylene) derivatives. *Nanoscale* 2020; **12**: 15150-15156
- 14 Hong W, Manrique DZ, Moreno-García P, *et al.* Single molecular conductance of tolanes: Experimental and theoretical study on the junction evolution dependent on the anchoring group. *J Am Chem Soc* 2012; **134**: 2292-2304
- 15 Hong W, Valkenier H, Mészáros G, *et al.* An mcbj case study: The influence of  $\pi$ -conjugation on the single-molecule conductance at a solid/liquid interface. *Beilstein J Nanotechnol* 2011; **2**: 699-713
- 16 Reddy P, Jang S-Y, Segalman RA, *et al.* Thermoelectricity in molecular junctions. *Science* 2007; **315**: 1568-1571
- 17 Soler J, Artacho E, Gale J, *et al.* The siesta method for ab initio order-n materials simulation. *J Phys Condens Matter* 2002; **14**:
- 18 Perdew JP, Burke K, Ernzerhof M. Perdew, burke, and ernzerhof reply. *Phys Rev Lett* 1998; **80**: 891-891
- 19 Ferrer J, Lambert C, García-Suárez V, *et al.* Gollum: A next-generation simulation tool for electron, thermal and spin transport. *New J Phys* 2014; **16**: 093029